THE JOURNAL OF PHYSICAL CHEMISTRY C

pubs.acs.org/JPCC Article

Direct Correlation of Mechanical Hardness and Chemical Bonding in Intermetallic Double Perovskite Borides $Sc_2Ir_{6-x}Pd_xB$

Published as part of The Journal of Physical Chemistry virtual special issue "Hellmut Eckert Festschrift".

Jan P. Scheifers, Raymond D.-T. Nguyen, Yuemei Zhang, and Boniface P. T. Fokwa*

Cite This: *J. Phys. Chem. C* 2020, 124, 26062−26067 Read Online

ACCESS | Metrics & More | Article Recommendations | Supporting Information

ABSTRACT: Atomic and/or vacancy ordering has proven to be important in understanding some unexpected properties in perovskites, leading to the formulation of double perovskites (oxides or halides) as a subclass of these compounds. Intermetallic double perovskite borides (IDPBs) have been described structurally, but the study of their physical properties is still in its infancy. In this work, we have investigated the mechanical hardness and microstructure of the series $Sc_2Ir_{6-x}Pd_xB$ for the first time. We found that the hardness decreases until $x = 5$, and then it levels off. This transition coincides with the change in structure from ordered to disordered. A detailed microstructure analysis reveals that the order−disorder transition at $x = 5$ is accompanied by the precipitation of small amounts of a boron-rich side phase. Interestingly, the hardness trend in the IDPBs ($x = 0$−4) is accurately reproduced by crystal orbital Hamilton populations (COHP) analysis, especially the total integrated COHP (iCOHP) which measures the bond strength in each compound. Furthermore, it is found that more antibonding states are occupied if Ir is replaced by alioelectronic Pd, thereby reducing the total iCOHP and thus explaining the reduced hardness with increasing Pd concentration.

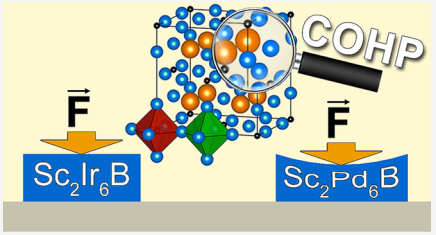

INTRODUCTION

In the past, valence electron counting (VEC) has been identified as a great tool to evaluate the stability not only of molecular-based compounds and complexes[1,2] but also of intermetallic compounds.[3,4] Some of those rules are purely empirical, and others are based on occupied orbitals. In the case of intermetallic perovskite borides (IPBs), Takeya *et al.* found that these compounds are stable within the range of 31 e^-/f.u. < VEC < 34.5 e^-/f.u.[5] Intermetallic boride perovskites can alternatively be described as Cu_3Au-type intermetallics (space group $Pm\bar{3}m$, see Figures 1A−C) with interstitial boron atoms (see Figures 1D−F).[6] In contrast to many other intermetallics, all interstitial (octahedral) sites can be occupied in boride perovskites, while most parent intermetallics exist without boron as well. Thus, the general composition of the IPBs is AT_3B_{1-y} (A: Au site and T: Cu site in Cu_3Au-type) with $0 \le y \le 1$. In 2006, boron-vacancy ordering was observed for the first time for $y = 0.5$ in $TiRh_3B_{1-y}$, which resulted in Ti_2Rh_6B.[7] The resulting $2 \times 2 \times 2$ superstructure Ti_2Rh_6B ($Fm\bar{3}m$) is isostructural to K_2PtCl_6, where boron atoms and vacancies (Pt^{4+} cations and vacancies in K_2PtCl_6) occupy the octahedral voids, alternatingly resulting in smaller and larger octahedra (see Figures 1G−I). Since then, ordering has been observed in many intermetallic boride perovskites.[8−12] Moreover, it was shown that the boron-vacancy ordering depends on the VEC, as an order−disorder transition was observed at 34 e^-/f.u. with the Fermi level (E_F) approaching the upper edge of the pseudogap in the density of states (DOS).[13]

Elemental boron is classified as a superhard refractory material with a hardness of 42 GPa for α-B_{12}.[14] The extraordinary hardness is a consequence of a 3D network of covalent B−B bonds. Intermetallic borides belong to the class of metallic refractory materials. Despite fewer covalent boron−boron bonds, many of these compounds are still hard or even superhard due to strong metal−boron bonds.[15−17] The correlation between hardness and boron concentration has been studied for IPBs since many of them provide a phase width allowing the boron concentration to be changed in a wide range.[9,18,19] In IPBs, no boron−boron bonds exist because the boron atoms are exclusively located in corner-sharing octahedra, which do not allow for boron−boron bonds. However, each boron-filled octahedron comes with six metal−boron bonds, causing the hardness to increase with increasing boron concentration. Interestingly, even before the discovery of boron ordering at $y = 0.5$, a sudden drop from the expected monotonous increase in the hardness in several solid−solution series AT_3B_{1-y} ($0 < y < 1$) was observed around $y = 0.5$. This sudden drop has been associated with the boron ordering and

Received: September 26, 2020
Revised: October 29, 2020
Published: November 13, 2020

https://dx.doi.org/10.1021/acs.jpcc.0c08773
J. Phys. Chem. C 2020, 124, 26062−26067

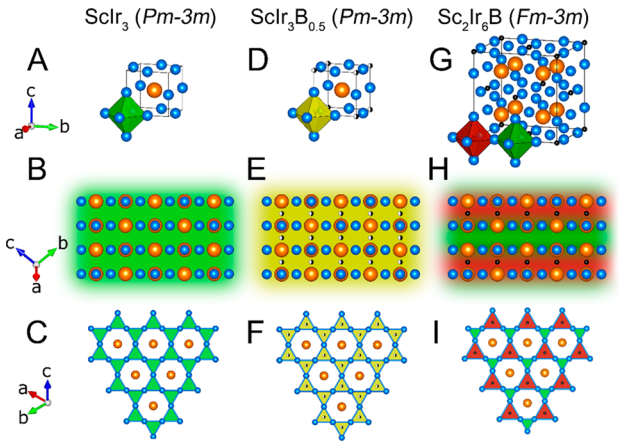

Figure 1. Comparison between Cu_3Au-type (A–C), perovskite-type (D, E), and ordered double perovskite-type (G–I) structures of $ScIr_3$, $ScIr_3B_{0.5}$, and Sc_2Ir_6B, respectively. Sc in orange, Ir in blue, and boron in black. Green, yellow, and red shadings represent empty, randomly distributed half-filled (with B), and B-filled Ir_6 octahedra, respectively. A cross section of each structure showing a layer-like arrangement (B, E, H) and the Kagomé layout (C, F, I) of said layers viewed along [111]. The different sizes of filled and empty octahedra of Sc_2Ir_6B in (I) are amplified.

the formation of a superstructure,[19] but no explanation has been proposed yet, an issue we have now addressed below. For clarity, we will refer to the disordered, primitive structure as $AT_3B_{0.5}$, while the ordered face-centered structure is denoted by using the formula A_2T_6B throughout the article.

The AT_3B_{1-y} structure can also be described as stacking of intersecting Kagome T-layers (stacking sequence –ABC–) along the [111] directions with A occupying the center of each hexagon (Figure 1F). The interstitial octahedral sites in the perovskite structure, where the boron atoms reside, are located between two of those layers, leading to the stacking sequence –AaBbCc–. In the case of the A_2T_6B superstructure, the T-atoms form a breathing Kagome lattice due to the presence of larger and smaller octahedra (Figure 1I). The boron atoms and vacancies alternate resulting in a different stacking sequence (–AaB□CcA□BbC□–), which leaves every other interstitial layer between the T-layers unoccupied (Figure 1H). We hypothesize that the unoccupied interstitial layers of the superstructure will allow gliding and therefore result in easier plastic deformation. In contrast, the disordered boron atoms in the simple structure will prevent the T-layers from gliding/slipping along each other, thereby increasing the hardness and brittleness even at lower boron concentrations. This is illustrated in the series $ScRh_3B_{1-y}$, in which the hardness of $ScRh_3B_{0.5}$ is only ca. 2 GPa, while the hardness of $ScRh_3B_{0.25}$ is roughly 4.5 GPa.[18] A previous density functional theory (DFT) study of $ScRh_3B_{1-y}$ found that at y = 0.5 the configuration which is isostructural to K_2PtCl_6 (ordered double perovskite) has the maximum bulk modulus.[20] However, the effects of the crystal structure on shear modulus and thus the overall hardness have not been studied yet. Ordering has been observed in other B-site vacant perovskites before such as $Cs_4BBi_2Cl_{12}$ (B = Mn and Cd), which similarly show preferential shearing,[21] and Cs_2SnI_6, which has a significantly lower charge carrier mobility than $CsSnI_3$.[22,23] Moreover, it was shown that ordering in the double perovskite oxide Sr_2FeMoO_6 strongly affects the physical properties such as the magnetoresistance.[24,25] Accordingly, ordered double perovskites are distinctly different from simple perovskites. Therefore, we hypothesize that the solid–solution series $Sc_2Ir_{6-x}Pd_xB$,[13] for which a transition from the ordered superstructure to the disordered simple structure was found, should show a sudden change in hardness around this transition. In the present work, we have performed DFT calculations to verify this hypothesis. Subsequently, we have investigated experimentally and theoretically the hardness of Sc_2Ir_6B as well as the effects of the VEC change and chemical bonding on hardness in the solid–solution series $Sc_2Ir_{6-x}Pd_xB$.

MATERIALS AND METHODS

Synthesis. The $Sc_2Ir_{6-x}Pd_xB$ (with x = 0, 2, 4, 5, and 6) samples were prepared by arc melting from the elements as previously described[13] and also given in the Supporting Information.

X-ray Diffraction Measurements. The synthesized bulk samples were crushed, and powder X-ray diffraction (PXRD) data were collected on a RIKAGU MiniFlex 600 benchtop diffractometer equipped with a graphite monochromator and a scintillation counter (SC-70) detector utilizing Cu Kα radiation (λ = 1.543 Å). PXRD measurements were also performed on samples used for the hardness measurements and the microstructure analysis.

Hardness Measurements. In preparation of the hardness measurements, the samples were sanded into disks (~0.5 mm in diameter) by using silicon carbide (SiC) sandpaper up to 1000 grit. Further polishing was then achieved via alumina particles with a diameter down to 1 μm. Hardness measurements were done on the Phase II Micro Vickers Hardness Tester Model 900-391. Using a square pyramid tip, we applied a test force of 0.49 N (50 g) with a dwell time of 15 s. A total of 25–35 indentations were performed on each sample to increase the statistical accuracy and certainty.

Electron Microscopy Measurements. Microstructure analysis was performed on a scanning electron microscope (SEM) FEI NovaNanoSEM 450 equipped with a field emitter gun (FEG) and a concentric backscattered detector (CBS) at an acceleration voltage of 20 kV. Energy dispersive X-ray spectroscopy (EDS) was also performed by using the same instrument to confirm sample composition and homogeneity.

Computational Methods. Elastic constants were calculated by using the projector augmented wave method of Blöchl[26] coded in the Vienna ab initio simulation package (VASP).[27,28] All VASP calculations employed the generalized gradient approximation (GGA) with exchange and correlation treated by the Perdew–Burke–Enzerhoff functional.[29] The convergence threshold for structural relaxation was set at 0.01 eV/Å in force. The cutoff energy for the plane wave calculations was set to 500 eV, and the Brillouin zone integrations were performed by using a 5 × 5 × 5 k-point mesh. Hill averaged bulk and shear moduli were calculated from the elastic constants obtained from VASP.[30,31] The Vickers hardness H_v was calculated by using the following equation: $H_v = 2(G^3/B^2)^{0.585} - 3$.[32] The DFT calculations were also performed by using the Stuttgart version of the tight-binding, linear muffin-tin orbital (TB-LMTO) method with atomic spheres approximation.[33] Within TB-LMTO, exchange and correlation were treated by using the von Barth–Hedin local density (LDA).[34] The basis sets include 4s/(4p)/3d wave functions for Sc, 6s/6p/5d/(5f) wave functions for Ir, and 2s/2p/(3d) wave functions for B with orbitals in parentheses treated by the Löwdin downfolding techniques.[35] Sets of 15 ×

https://dx.doi.org/10.1021/acs.jpcc.0c08773
J. Phys. Chem. C 2020, 124, 26062–26067

15 × 15 k-points were used for integrations involving the irreducible wedge of the cubic Brillouin zone. The electronic structure calculations were based on the crystal structure of ordered Sc_2Ir_6B, and the results for different VEC were obtained by applying the rigid band approximation (RBA). Chemical bonding was evaluated in terms of crystal orbital Hamilton populations (COHP).[36] The integrated COHP (iCOHP) reflects the bond strength. iCOHP values are obtained by integrating the COHP of each bond up to the Fermi level. The net total iCOHP per formula unit of a compound is then the total of all iCOHPs multiplied by their respective count per formula unit.

RESULTS AND DISCUSSION

VASP calculations were employed to evaluate the bulk modulus, shear modulus, and Vickers hardness of ordered Sc_2Ir_6B (Figure 1G) in comparison with those of its disordered configuration (Figure 2). Four structure models (Table 1) were used to calculate the elastic constants: A fixed volume (experimental) and a fully optimized volume were used in each case (ordered and disordered Sc_2Ir_6B). Both bulk and shear moduli were found to be smaller for the fully optimized structures if compared to the corresponding fixed volume ones because of the larger cell parameters. It is obvious that the shear modulus increases from the ordered to disordered structure, which supports our hypothesis that the covalent metal−boron bonds between the T-layers prevent them from gliding/sliding along each other in the disordered structure. The overall calculated Vickers hardness is by 1.0 or 1.6 GPa (for fixed or optimized volume, respectively) smaller for the ordered structure, a result reminiscent of the hardness drop previously found experimentally for the $ScRh_3B_{1-x}$ series where the only ordered member (x = 0.5) had the lowest hardness.[9,37] Therefore, the order−disorder transition should increase the hardness of IPBs. A finding that sparked the following theoretical and experimental hardness studies of the series $Sc_2Ir_{6-x}Pd_xB$.

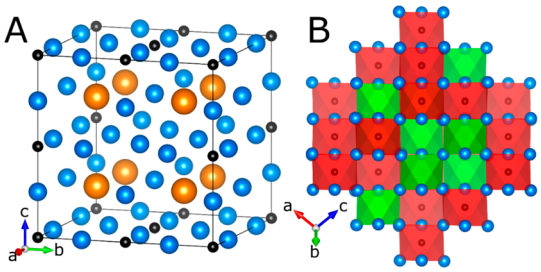

Figure 2. Unit cell configuration used to simulate disordered Sc_2Ir_6B (A). Projection of layers build of fully occupied (red) and completely empty (green) octahedra (B).

Table 1. Bulk Modulus B_H, Shear Modulus G_H, and Vickers Hardness H_V of Ordered and Disordered Sc_2Ir_6B (V Is the Experimental Volume)

model	cell parameters (Å)	B_H (GPa)	G_H (GPa)	H_V (GPa)
ordered Sc_2Ir_6B (fixed V)	a = 7.965	156.2	96.4	13.5
disordered Sc_2Ir_6B (fixed V)	a = 7.965	157.9	100.4	14.5
ordered Sc_2Ir_6B (optimized)	a = 8.053	139.6	85.8	12.3
disordered Sc_2Ir_6B (optimized)	a = 8.073	135.3	88.9	13.9

According to the recorded PXRD patterns (Figure SI1), the $Sc_2Ir_{6-x}Pd_xB$ samples with x = 0−5 show superstructure reflections while none is found for x = 6 (disordered $ScPd_3B_{0.5}$), thus corroborating previous reports.[12,38] Furthermore, the homogeneity of the $Sc_2Ir_{6-x}Pd_xB$ samples was checked by EDS mapping (Figure SI1), which showed a uniform spatial distribution of the elements for all samples except for x = 6 (discussed in detail in the microstructure study below). The measured hardness decreases monotonously with increasing x from 9.27(2) GPa for Sc_2Ir_6B (x = 0) down to 5.88(6) GPa for x = 5, and then it levels off (see Figure 3 and Table 2). Because the IPBs studied here are cubic, anisotropy and a preferred orientation of the grains do not have a significant impact on the hardness measurements. Thus, the decreasing hardness with increasing x (or increasing Pd content) can be solely attributed to the intrinsic effects of Pd substitution for Ir. To explain these findings, the electronic structure and a detailed chemical bonding analysis were carried out.

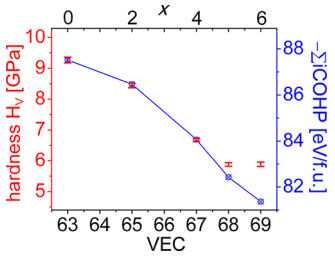

Figure 3. Experimental Vickers hardness (H_V) and total iCOHP vs VEC and x in the series $Sc_2Ir_{6-x}Pd_xB$.

Table 2. Vickers Hardness H_V of Selected Borides with the Respective Load Applied

boride	H_V (GPa)	load (N)	ref
WB_4	28.1(1.4)	4.9	40
Fe_2B	18.14	2.9	41
Mn_3B_4	16.3	4.9	42
MnB	15.7	4.9	43
RuB	8.0(8)	4.9	44
$ScRh_3B$	9.9(1)	2.9	37
$CeRh_3B$	6.5(2)	2.9	18
$LaRh_3B$	4.2(1)	2.9	37
$ScRh_3$	1.9(1)	2.9	45
$CeRh_3$	2.0(1)	2.9	18
Sc_2Ir_6B	9.27(7)	4.9	this work
$Sc_2Ir_4Pd_2B$	8.44(7)	4.9	this work
$Sc_2Ir_2Pd_4B$	6.68(5)	4.9	this work
Sc_2IrPd_5B	5.88(6)	4.9	this work

The calculated density of states (DOS) of Sc_2Ir_6B shows a deep pseudogap (Figure 4) at E_F, hinting at its electronic stability. According to the rigid-band model (RBM), substituting Ir by alioelectronic Pd would shift E_F toward the upper edge of the pseudogap. To verify that the RBM is valid for these phases, we have also calculated the DOS of hypothetical "Sc_2Pd_6B" (Figure SI3), the result of which validates the RBM, as its DOS is nearly identical with that of

https://dx.doi.org/10.1021/acs.jpcc.0c08773
J. Phys. Chem. C 2020, 124, 26062−26067

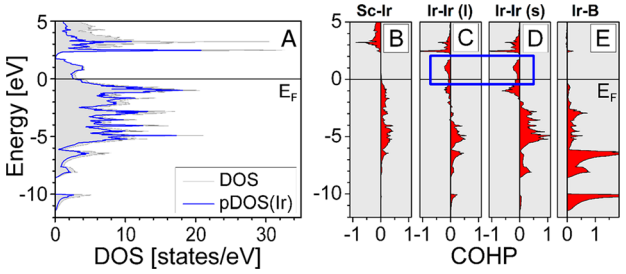

Figure 4. Density of states of Sc_2Ir_6B with partial DOS of Ir (A) and COHP curves (B–E) for the Sc–Ir (B), the long Ir–Ir (C), the short Ir–Ir (D), and the Ir–B (E) bonds. The Fermi level (E_F) was set to 0 eV. The blue box in panels C and D highlights the antibonding Ir–Ir interactions in the pseudogap. By increasing the VEC in hypothetical Sc_2Pd_6B, the E_F shifts slightly above +2 eV if compared to E_F of Sc_2Ir_6B.

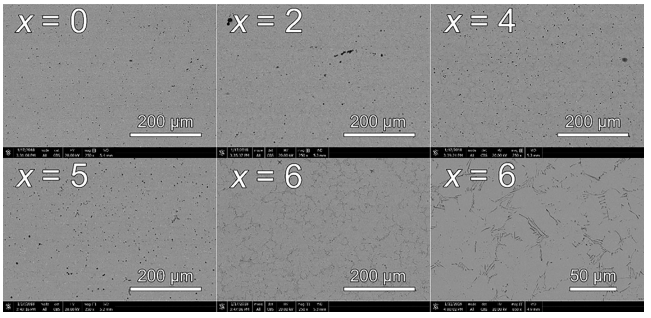

Figure 5. Backscattered-electron (BSE) images showing the microstructure for all five $Sc_2Ir_{6-x}Pd_xB$ samples (x = 0, 2, 4, 5, and 6) and a higher magnification image of the last sample with x = 6, where we can clearly see the precipitation of ScB_2 platelets. All microstructures also exhibit circular black spots, which are voids that occur during solidification.

Sc_2Ir_6B, the only notable difference being the expected E_F shift due to the additional valence electron (VE) of Pd.

Analyzing the Sc_2Ir_6B COHP curves of the Sc–Ir, the long Ir–Ir, the short Ir–Ir, and the Ir–B interactions (Figure 4), we find that the interactions in the entire pseudogap are predominantly antibonding Ir–Ir interactions. Thus, shifting the Fermi level by increasing x (increasing VEs) will add more antibonding Ir–Ir interactions, thereby decreasing the overall bond strength and thus the hardness. Indeed, as can be seen in Figure 3, the total iCOHP per formula unit (f.u.) in the series decreases with increasing x from 87.5 eV/f.u. (x = 0) to 81.4 eV/f.u. (x = 6). Astonishingly, the decrease of the total iCOHP/f.u. overlaps perfectly with the decrease of the Vickers hardness (see Figure 3) from x = 0 to x = 4, and then both curves deviate. While the deviation is small for x = 5, it becomes quite large for x = 6 because the Vickers hardness is basically the same for these two compositions. In fact, by extrapolation (using the iCOHP curve in Figure 3) a Vickers hardness of ca. 4.55 GPa would have been expected for x = 6 instead of the experimental 5.88(6) GPa if no structure change had occurred. This result corroborates the above finding (using Sc_2Ir_6B) that a disordered perovskite structure ($ScPd_3B_{0.5}$, x = 6) would be harder than an ordered one (hypothetical "Sc_2Pd_6B").

The hardness of materials is affected by both intrinsic (chemical bonding dependent) and extrinsic (microstructure dependent) properties. We have discussed the direct relationship between chemical bonding and hardness in $Sc_2Ir_{6-x}Pd_xB$ above. Now, we will focus on the influence of the microstructure on hardness in this series. The samples x = 0, 2, 4, and 5 have similar microstructures (Figure 5) with smooth surfaces and good homogeneities, which distinguishes them from the sample x = 6 that shows inclusions of a secondary phase. These results point to a negligible influence of microstructure on the hardness differences for x = 0, 2, 4, and 5. Consequently, mainly the intrinsic effects would induce a change in hardness for these samples, thereby explaining the good agreement found between hardness and total iCOHP (Figure 3). The microstructure of sample x = 6 reveals the precipitation of a phase that was not detected by PXRD. While EDS cannot reliably quantify the amount of boron, Sc and B were found in the side phase. Thus, the most likely compound for the precipitate according to the binary Sc–B phase diagram is ScB_2.[38] The precipitation of ScB_2 has important implications for the x = 6 sample. It explains the presence of minor amounts of Pd found in previous studies,[12,38] which can be detected by PXRD contrary to the minor ScB_2 because the X-rays' sensitivity of Pd is much higher due to the higher average atomic number [$\bar{Z}$(Pd) = 46, $\bar{Z}$(ScB_2) = 10.3]. Because ScB_2 is a boron-rich compound, less boron is available to be incorporated into the perovskite after its precipitation, leading to a boron-deficient phase, $ScPd_3B_y$ (y < 0.5). The boron deficiency does not allow for alternating boron-vacancy ordering, and consequently the 2 × 2 × 2 superstructure is not observed for x = 6. This conclusion corroborates previous solid-state NMR results, which showed a large difference between the ^{11}B spectra for x = 6 and other x < 6 samples.[39]

Let us look at the impact of boron deficiency on the hardness. We concluded above through iCOHP analysis that disordered $ScPd_3B_{0.5}$ (x = 6) would be harder than ordered hypothetical "Sc_2Pd_6B". However, this analysis considered neither boron deficiency nor extrinsic effects. With the boron concentration decreasing below y = 0.5 when moving from x = 5 to x = 6, the hardness for x = 6 is difficult to assess. The Fermi level may not shift when moving from x = 5 to x = 6 because the increase in VEC (increasing Pd) may be compensated by the decrease in boron concentration. However, the total iCOHP per formula unit changes due to fewer Pd–B bonds, thereby lowering the intrinsic hardness of the x = 6 sample. Nevertheless, the disordered structure should increase the intrinsic hardness according to our above-demonstrated model. Finally, the precipitation of ScB_2 also affects the microstructure and the mechanical properties. Overall, all these different aspects affecting the hardness cancel out, leading to a nearly identical hardness for x = 5 and x = 6 (Figure 3). Overall, the studied materials have lower Vickers hardness values than the boron-rich borides but higher values than the reported metal-rich borides so far at identical applied loads (Table 2).

CONCLUSION

We have studied the effect of boron ordering on the hardness of Sc_2Ir_6B by density functional theory (DFT) calculations. We found that the overall calculated Vickers hardness is smaller for an ordered structure. We then studied the effect of Pd substitution for Ir on the hardness in the series $Sc_2Ir_{6-x}Pd_xB$ and found that the hardness decreases from x = 0 until x = 5, and then it levels off. Chemical bonding analysis, using the crystal orbital Hamilton populations (COHP) and the total integrated COHP per formula unit (iCOHP/f.u.), showed that most of the states within the large pseudogap of Sc_2Ir_6B are

https://dx.doi.org/10.1021/acs.jpcc.0c08773
J. Phys. Chem. C 2020, 124, 26062–26067

dominated by antibonding Ir−Ir interactions. Thus, shifting the Fermi level within the pseudogap toward its upper edge (by substituting Ir with Pd) will add more antibonding states and reduce the total iCOHP/f.u. (bond strength), thereby lowering the hardness. Moreover, the microstructure analysis revealed smooth surfaces for the x = 0−5 samples, while precipitation of a minor boron-rich side phase was observed for x = 6, an indication that the solubility limit of boron has been exceeded for $ScPd_3B_{0.5}$ (x = 6). The combined effects of chemical bonding, order−disorder transition, and microstructure result in a hardness level off for $x \geq 5$ in the series $Sc_2Ir_{6-x}Pd_xB$.

■ ASSOCIATED CONTENT

Supporting Information

The Supporting Information is available free of charge at https://pubs.acs.org/doi/10.1021/acs.jpcc.0c08773.

Synthesis details, X-ray powder diffraction data, SEM and EDX data, and DOS of hypothetical Sc_2Pd_6B (PDF)

■ AUTHOR INFORMATION

Corresponding Author

Boniface P. T. Fokwa − *Department of Chemistry and Bourns College of Engineering, University of California, Riverside, Riverside, California 92521, United States;* orcid.org/0000-0001-9802-7815; Email: bfokwa@ucr.edu

Authors

Jan P. Scheifers − *Department of Chemistry, University of California, Riverside, Riverside, California 92521, United States*

Raymond D.-T. Nguyen − *Bourns College of Engineering, University of California, Riverside, Riverside, California 92521, United States*

Yuemei Zhang − *Department of Chemistry, University of California, Riverside, Riverside, California 92521, United States;* orcid.org/0000-0003-1574-2931

Complete contact information is available at: https://pubs.acs.org/10.1021/acs.jpcc.0c08773

Author Contributions

J.P.S. and R.D.-T.N. fabricated the samples and performed the experiments. Y.Z. performed the computational calculations. J.P.S. wrote the manuscript with support from Y.Z. and B.P.T.F. B.P.T.F encouraged J.P.S. to investigate boride perovskites and supervised the project. All authors discussed the results and commented on the manuscript.

Notes

The authors declare no competing financial interest.

■ ACKNOWLEDGMENTS

This work was mainly supported by B.P.T.F.'s startup funds provided by UC Riverside and partial funding by the NSF Career award to B.P.T.F. (DMR-1654780). Additional support by the UC Riverside's dissertation year award to J.P.S. is acknowledged. The authors thank Suveen N. Mathaudhu and Trevor Clark for their advice and access to the hardness tester. The authors also gratefully acknowledge the San Diego Supercomputer Center (SDSC) for providing computing resources.

■ REFERENCES

(1) Wade, K. The structural significance of the number of skeletal bonding electron-pairs in carboranes, the higher boranes and borane anions, and various transition-metal carbonyl cluster compounds. *J. Chem. Soc. D* **1971**, 792−793.

(2) Mingos, D. M. P. A General Theory for Cluster and Ring Compounds of the Main Group and Transition Elements. *Nature, Phys. Sci.* **1972**, *236*, 99−102.

(3) Schäfer, H.; Eisenmann, B.; Müller, W. Zintl Phases: Transitions between Metallic and Ionic Bonding. *Angew. Chem., Int. Ed. Engl.* **1973**, *12*, 694−712.

(4) Yannello, V. J.; Fredrickson, D. C. Generality of the 18-n Rule: Intermetallic Structural Chemistry Explained through Isolobal Analogies to Transition Metal Complexes. *Inorg. Chem.* **2015**, *54*, 11385−11398.

(5) Takeya, H.; Shishido, T.; Takei, H. Studies on the perovskite solid solution Er(Rh, M)3By (M ≡ Pd, Pt and 0 ≤ y ≤ 1). *J. Less-Common Met.* **1987**, *134*, 263−273.

(6) Bodak, O.; Demchenko, P.; Seropegin, Y.; Fedorchuk, A. Cubic structure types of rare-earth intermetallics and related compounds. *Z. Kristallogr. - Cryst. Mater.* **2006**, *221*, 482−492.

(7) Fokwa, B. P. T.; Eck, B.; Dronskowski, R. Ti2Rh6B - a new boride with a double perovskite-like structure containing octahedral Rh6 cluster. *Z. Kristallogr. - Cryst. Mater.* **2006**, *221*, 445−449.

(8) Yubuta, K.; Nomura, A.; Nakajima, K.; Shishido, T. Crystal structure of a Cu3Au-type compound CeRh3B0.5 studied by high-resolution electron microscopy. *J. Alloys Compd.* **2006**, *426*, 308−311.

(9) Yubuta, K.; Nomura, A.; Nakajima, K.; Shishido, T. Structural variations of ScRh3Bx (x = 0−1) phase studied by transmission electron microscopy. *J. Alloys Compd.* **2009**, *471*, 341−346.

(10) Zeiringer, I.; et al. Crystal structure and Ce valence variation in the solid solution CeRh 3 − x Pd x B 0.5. *Mater. Res. Express* **2014**, *1*, 016101.

(11) Yubuta, K.; et al. Nanostructure with diffuse streaks in ScRh3B0.6 compound studied by electron microscopy. *Solid State Sci.* **2020**, *102*, 106177.

(12) Hermus, M.; Fokwa, B. P. T. Zr2Ir6B with an eightfold superstructure of the cubic perovskite-like boride ZrIr3B0.5: Synthesis, crystal structure and bonding analysis. *J. Solid State Chem.* **2010**, *183*, 784−788.

(13) Hermus, M.; Scheifers, J. P.; Touzani, R.; Fokwa, B. P. T. Electronic pseudogap-driven formation of new double-perovskite-like borides within the Sc2Ir6-xTxB (T = Pd, Ni; X = 0−6) series. *Inorg. Chem.* **2015**, *54*, 4056.

(14) Amberger, E.; Stumpf, W. *Boron* **1981**, 112−238.

(15) Chung, H. Y.; et al. Synthesis of ultra-incompressible superhard rhenium diboride at ambient pressure. *Science (Washington, DC, U. S.)* **2007**, *316*, 436−439.

(16) Levine, J. B.; Tolbert, S. H.; Kaner, R. B. Advancements in the Search for Superhard Ultra-Incompressible Metal Borides. *Adv. Funct. Mater.* **2009**, *19*, 3519−3533.

(17) Yeung, M. T.; Mohammadi, R.; Kaner, R. B. Ultra-incompressible, Superhard Materials. *Annu. Rev. Mater. Res.* **2016**, *46*, 465−485.

(18) Shishido, T.; et al. Boron nonstoichiometry, hardness and oxidation resistance of perovskite-type CeRh3Bx (x = 0−1). *J. Alloys Compd.* **2006**, *426*, 304−307.

(19) Yubuta, K.; Nomura, A.; Yamamura, T.; Shishido, T. Anomalous behavior of hardness and crystal structure in CeRh3Bx (x = 0−1) phase. *J. Alloys Compd.* **2008**, *451*, 301−304.

(20) Sahara, R.; et al. Mechanism of the increase in bulk modulus of perovskite Sc Rh3 Bx by vacancies. *Phys. Rev. B: Condens. Matter Mater. Phys.* **2006**, *73*, 184102.

(21) Holzapfel, N. P.; Majher, J. D.; Strom, T. A.; Moore, C. E.; Woodward, P. M. Cs 4 Cd 1− x Mn x Bi 2 Cl 12 —A Vacancy-Ordered Halide Perovskite Phosphor with High-Efficiency Orange-Red Emission. *Chem. Mater.* **2020**, *32*, 3510−3516.

(22) Saparov, B.; et al. Thin-Film Deposition and Characterization of a Sn-Deficient Perovskite Derivative Cs2SnI6. *Chem. Mater.* **2016**, *28*, 2315−2322.
(23) Maughan, A. E.; Ganose, A. M.; Scanlon, D. O.; Neilson, J. R. Perspectives and Design Principles of Vacancy-Ordered Double Perovskite Halide Semiconductors. *Chem. Mater.* **2019**, *31*, 1184−1195.
(24) Sarma, D. D.; et al. Magnetoresistance in ordered and disordered double perovskite oxide, Sr2FeMoO6. *Solid State Commun.* **2000**, *114*, 465−468.
(25) Moritomo, Y.; et al. Effects of B-site disorder in Sr2FeMoO6 with double perovskite structure. *Japanese J. Appl. Physics, Part 2 Lett.* **2001**, *40*, L672.
(26) Blöchl, P. E. Projector augmented-wave method. *Phys. Rev. B: Condens. Matter Mater. Phys.* **1994**, *50*, 17953−17979.
(27) Kresse, G. Vienna ab initio simulation package, 1999.
(28) Kresse, G.; Hafner, J. Ab initio molecular dynamics for liquid metals. *Phys. Rev. B: Condens. Matter Mater. Phys.* **1993**, *47*, 558−561.
(29) Perdew, J. P.; Burke, K.; Ernzerhof, M. Generalized Gradient Approximation Made Simple. *Phys. Rev. Lett.* **1996**, *77*, 3865−3868.
(30) Hill, R. The elastic behaviour of a crystalline aggregate. *Proc. Phys. Soc., London, Sect. A* **1952**, *65*, 349−354.
(31) Hill, R. Elastic properties of reinforced solids: Some theoretical principles. *J. Mech. Phys. Solids* **1963**, *11*, 357−372.
(32) Chen, X. Q.; Niu, H.; Li, D.; Li, Y. Modeling hardness of polycrystalline materials and bulk metallic glasses. *Intermetallics* **2011**, *19*, 1275−1281.
(33) Tank, R. W.; Jepsen, O. The STUTTGART TB-LMTO-ASA program. *Cell* **1998**, 1−27.
(34) Von Barth, U.; Hedin, L. A local exchange-correlation potential for the spin polarized case. I. *J. Phys. C: Solid State Phys.* **1972**, *5*, 1629−1642.
(35) Lowdin, P.-O. A Note on the Quantum-Mechanical Perturbation Theory. *J. Chem. Phys.* **1951**, *19*, 1396−1171.
(36) Dronskowski, R.; Bloechl, P. E. Crystal orbital Hamilton populations (COHP): energy-resolved visualization of chemical bonding in solids based on density-functional calculations. *J. Phys. Chem.* **1993**, *97*, 8617−8624.
(37) Shishido, T.; et al. Synthesis, boron-nonstoichiometry and hardness of perovskite-type rare earth rhodium borides RRh3Bx (R = La, Gd, Lu and Sc). *J. Alloys Compd.* **2006**, *408*−*412*, 379−383.
(38) Spear, K. E.; Uao, P. K. The B-Sc (Boron-Scandium) System.
(39) Koumoulis, D.; Scheifers, J. P.; St. Touzani, R.; Fokwa, B. P. T.; Bouchard, L. Direct Chemical Fine-Tuning of Electronic Properties in Sc2Ir6−xPdxB. *ChemPhysChem* **2016**, *17*, 2972.
(40) Mohammadi, R.; et al. Enhancing the Hardness of Superhard Transition-Metal Borides: Molybdenum-Doped Tungsten Tetraboride. *Chem. Mater.* **2016**, *28*, 632−637.
(41) Ma, S.; et al. Effect of crystal orientation on microstructure and properties of bulk Fe2B intermetallic. *J. Mater. Res.* **2015**, *30*, 257−265.
(42) Ma, S.; et al. Double-zigzag boron chain-enhanced Vickers hardness and manganese bilayers-induced high d-electron mobility in Mn3B4. *Phys. Chem. Chem. Phys.* **2019**, *21*, 2697−2705.
(43) Ma, S.; et al. Manganese mono-boride, an inexpensive room temperature ferromagnetic hard material. *Sci. Rep.* **2017**, *7*, 1−9.
(44) Gu, Q.; Krauss, G.; Steurer, W. Transition Metal Borides: Superhard versus Ultra-incompressible. *Adv. Mater.* **2008**, *20*, 3620−3626.
(45) Shishido, T. Synthesis, boron-nonstoichiometry and hardness of perovskite-type rare earth rhodium borides RRh3Bx (R = La, Gd, Lu and Sc). *J. Alloys Compd.* **2006**, *408*−*412*, 379−383.

https://dx.doi.org/10.1021/acs.jpcc.0c08773
J. Phys. Chem. C 2020, 124, 26062−26067